Supporting Information

Plasmonic Heating by Indium Tin Oxide Nanoparticles:

Spectrally Enabling Decoupled Near-Infrared Theranostics

Nicol Caetano-Zeballos[a,b], Leyre Aldaz-Caballero[a], Jesús Giráldez-Martínez[c], Lucas V. Besteiro[c], Marta Quintanilla[d,f], Riccardo Marin*[a,e], and Antonio Benayas*[a,b,f]

Table of Contents

S1. Synthesis

Synthesis parameters of ITO NPs

Table S1. Parameters investigated for the synthesis of ITO NPs (%Sn^{4+} and organic acid ligand). The sample highlighted in blue has been used for the transfer to water, HCE measurements and proof-of-concept experiment of the work.

Sample	*%Sn*	REAGENTS AND SOLVENTS					T (ºC)	t (h)
		OE (mL)	$In(OA)_3$ (mmol)	OM (mmol)	Sn-HHN (mmol)	BA/OcA (mmol)		
ITO-5	5	5	0.57	5	0.03	1.8	280	5
ITO-10	10	5	0.54	5	0.06	1.8	280	5
ITO-15	15	5	0.51	5	0.09	1.8	280	5
ITO-20	20	5	0.48	5	0.12	1.8	280	5

Synthesis of sodium citrate-capped CuS NPs

The synthesis procedure of citrate-capped CuS NPs was adapted from a protocol reported by Chen.F et al.[1] Ten mL of $CuCl_2 \cdot 2H_2O$ (0.006 mM) and 10 mL of sodium citrate (0.004 mM) were added in a 50-mL three-neck round-bottom flask. The mixture was stirred for 30 min at room temperature. Subsequently, 50 μL of $Na_2S \cdot 9H_2O$ (61.9 mM) was added to the mixture and stirred for another 5 min (the solution turned dark brown immediately). The flask was then transferred to an oil bath preheated at 90 ºC and kept at that temperature for 15 min. The obtained dark green NP dispersion was transferred to a vial and stored in at 8 ºC.

Preparation of 0.2 M gadolinium acetate $Gd(CH_3COO)_3$ in water

Following a previous work that reported the synthesis of $Gd(CH_3COO)_3$ [2], a 362.5 mg (1 mmol) of Gd_2O_3 , 1.5 mL (26.2 mmol) of acetic acid and 1.5 mL of distilled water were mixed in a Pyrex microwave reaction vessel. The vial was capped and placed in a microwave reactor (CEM Discover 2.0). The heating program entails the following steps: i) ramp to 180 ºC in 5 min, ii) hold at 180 ºC for 30 min, iii) rapid cooling to 70 ºC. The resulting solution was transferred to a 50-mL three-neck round-bottom flask, which was placed in an oil bath preheated at 60 ºC and kept at that temperature for 24 h to dry. Finally, the obtained white powder was dissolved in 10 mL of distilled water with 150

μL of acetic acid until complete redispersion. For the preparation of $Nd(CH_3COO)_3$, the same procedure was followed substituting Gd_2O_3 for Nd_2O_3.

Synthesis of $NaGdF_4$:Nd^{3+}/$NaGdF_4$ core-shell in hexane

The synthesis protocol for the synthesis of core $NaGdF_4$ nanoparticles doped with 5% of Nd^{3+} was adapted from a previous work.[2] A total of 1.95 mL of 0.2 M $Gd(CH_3COO)_3$ stock solution, 50 μL of 0.2 M $Nd(CH_3COO)_3$ stock solution, 4 mL of oleic acid (OA) and 6 mL of 1-octadecene (ODE) were added into a 50-mL three-neck round-bottom flask that was placed in a heating mantle. The mixture was heated at 150 ºC and kept at that temperature for 40 min under stirring. The flask was removed from the heating mantle, and the transparent yellow solution was allowed to naturally cool down to room temperature while stirring. Subsequently, 1 mL of a 1 M NaOH stock solution and 3.3 mL of a 0.4 M NH_4F stock solution – both prepared in methanol – were transferred to a 15-mL centrifuge tube and shaken by vortex for 10 s. This mixture was quickly added into the reaction flask to prevent precipitation of NaF. The resulting turbid yellow solution was transferred to an oil bath preheated at 50 ºC, in which it was kept at that temperature for 30 min. After connecting the flask to a Schlenk line, the solution was kept at 100 ºC and under vacuum for 10 min. Then, the solution degassed mixture was flushed with Ar, and the temperature was increased to 280 ºC and kept for 1.5 h. After this time, the flask was removed from the heating mantle, letting the dark brown dispersion cool down to room temperature while stirring. The resulting dispersion was transferred to 15-mL centrifuge tubes, which 5 mL of ethanol were also added. The mix was centrifuged for 3 min at 3500 rcf. The supernatant was then discarded, and the NPs were redispersed in 4 mL of hexane, followed by the addition of 8 mL of ethanol to induce the precipitation of the NPs, during further centrifugation steps. This process was repeated one more time, replacing the 8 mL of ethanol with a mixture of 4 mL of ethanol and 4 mL of methanol. After discarding the supernatant, the obtained core NPs were redispersed in 4 mL of hexane, resulting in a transparent yellow dispersion.

For the core-shell NPs synthesis, the procedure of the same previously reported work was followed. A 2 mL of 0.2 M $Gd(CH_3COO)_3$ stock solution, 4 mL of OA and 6 mL of ODE were added to a 50 mL three-neck round-bottom flask placed in a heating mantle. The mixture solution was heated at 150 ºC and kept at that temperature for 40 min under stirring. The flask was removed from the heating mantle and the transparent yellow

solution was allowed to naturally cool down to room temperature while stirring. Subsequently, the 4 mL of core NP dispersion in hexane previously synthesized was added into the flask along with a mixture of 1 mL of 1M NaOH stock solution and 3.3 mL of 0.4 M NH_4F stock solution, both prepared in methanol. After this, the following steps were repeated following the core NPs protocol described in this section.

S2. Comparison of FTIR spectra of Indium precursors

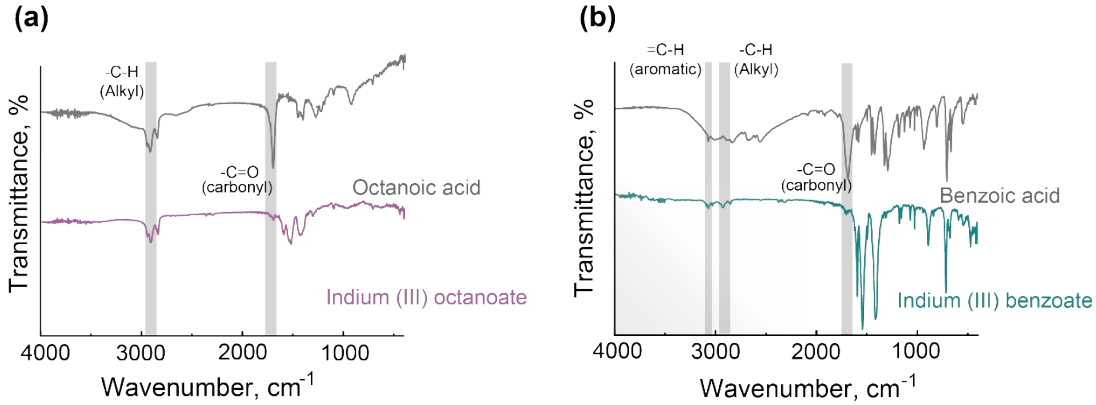

Figure S1. FTIR and offset spectra of the precursors: (a) octanoic acid (OcA, grey line) and indium (III) octanoate (pink line). (b) benzoic acid (BA, grey line) and indium (III) benzoate (blue line). As expected, around 3000 cm^{-1} only the vibrations of alkyl groups are observed for octanoic acid and In-octanoate, while also aryl groups are observed in the spectrum of benzoic acid and In-benzoate. In both complexes, the stretching around 1700 cm^{-1} arising from the carbonyl group shifts to lower wavenumbers due to the interaction with the metal ion, which changes the resonance frequency of the C=O vibration. The region < 1500 cm^{-1} in the spectra of both complexes show the main vibrations also observed in the spectra of the respective pure acids. Overall, these results confirm the nature of the two In^{3+} complexes.

S3. Structural characterization of ITO NPs

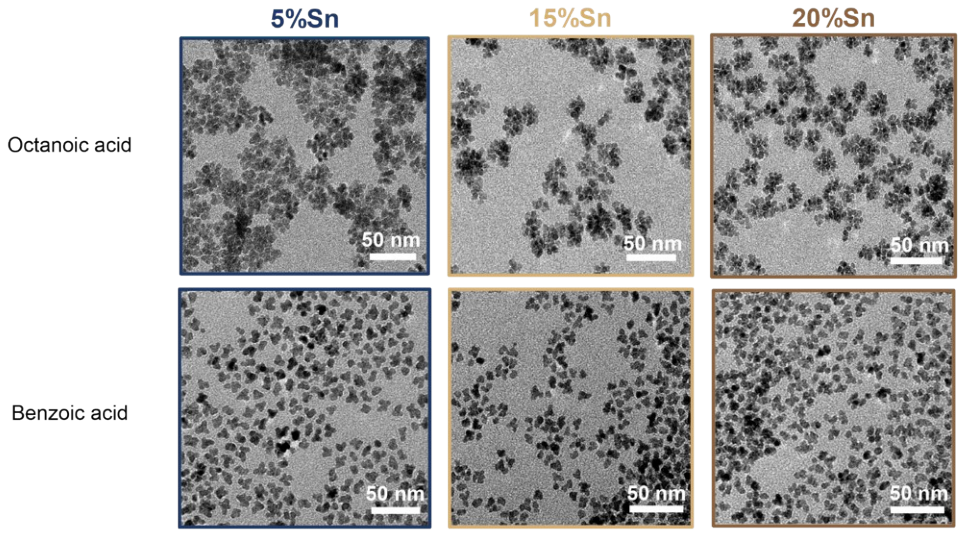

Figure S2. Representative TEM images of ITO NPs using different Sn concentrations (5, 15 and 20%) and different organic acid ligands in the synthesis: octanoic acid (OcA, top) benzoic acid (BA, bottom).

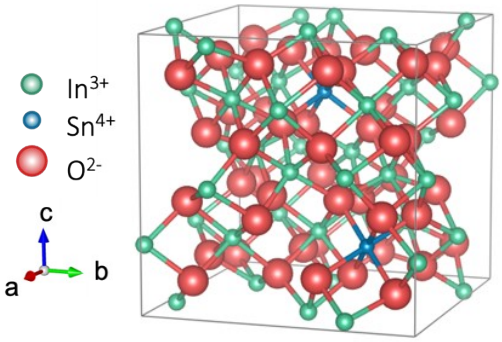

Figure S3. Diagram of the ITO crystal structure.

The X-ray diffractograms (**Figure S4**) show the crystalline structure of the ITO NPs with different Sn^{4+} concentrations. The XRD patterns were consistent with the pattern of the cubic structure of bixbyite (PDF # 04-010-3287).

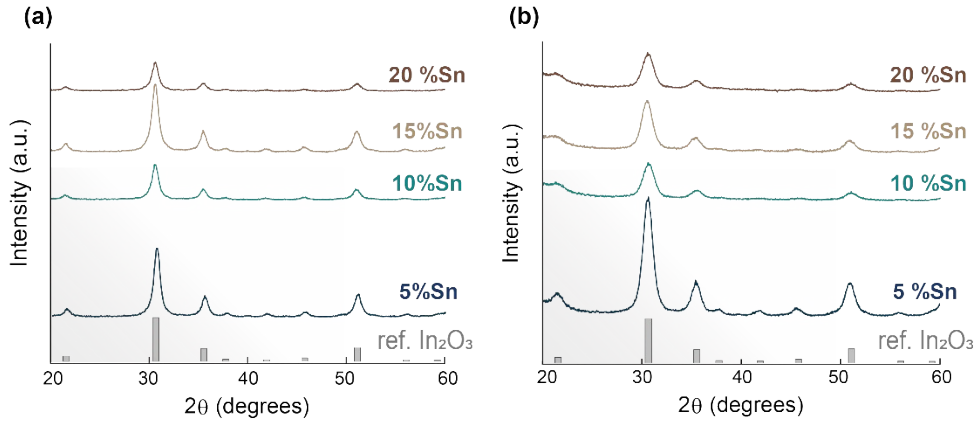

Figure S4. X-ray diffraction patterns of ITO NPs using different Sn concentrations (5,10, 15 and 20%) and different organic acid ligands in the synthesis: Benzoic acid (a) and octanoic acid (b). The In_2O_3 reference pattern is also provided (PDF # 04-010-3287). Data were plotted with a vertical offset for clarity.

A shift of the peaks with increasing Sn^{4+} concentration (incorporation of the Sn^{4+} ion with a smaller ionic radius than the host In^{3+} ions) was expected, although no such shift was observed. This is likely because of a partial introduction of Sn^{4+} into ITO structure, with respect to the quantities used during the synthesis process. The incorporation efficiency of dopant ions is very rarely 100% unless the substitutive ion matches very well in charge the substituted one. This is clearly not the case with In^{3+} and Sn^{4+}. In fact, defects should be included to maintain charge compensation alongside a lattice distortion to accommodate the dopant, then deviating heavily from the perfect crystal structure. (In other words, there's some "resistance" of the material to get more distorted, thus imposing an upper threshold to the fraction of available Sn^{4+} to be effectively incorporated into the ITO lattice).

S4. TXRF measurements

Samples synthesized in two series, with BA or OcA, with different Sn^{4+} concentrations between 5 and 20% have been analyzed *via* total reflection X-ray fluorescence (TXRF).

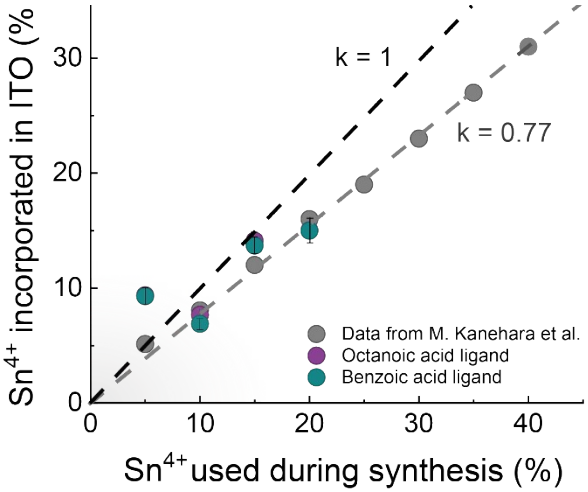

Figure S5. Percentage of Sn^{4+} incorporated into ITO NPS crystalline lattice as a function of the Sn^{4+} mass percentage fed into the synthesis, for samples synthesized with octanoic (purple dots) or benzoic acid (blue dots). The trend is compared to the data from Kanehara et al.[3] showing a good agreement. Dashed lines represent the incorporation rate, *k*: the black line is a 100% incorporation (k = 1), and the gray one is a linear fit of the data, (k = 0.77).

The incorporation efficiency, k, defined as the ratio of Sn^{4+} incorporated into de material versus the concentration added to the synthesis $k = {}^{Sn^{4+}_{incorporated}}/_{Sn^{4+}_{feed\ into\ synth}}$ can be obtained from the slope of a linear fitting of data in **Figure S5**. In this synthesis, our experimental *k* is clearly lower than 1. Moreover, taking the data of Kanehara et al[3] as reference, we can see that they largely match our data, and thus that k can be assumed to be 0.77 (77%).

S5. Optical properties of ITO NPs

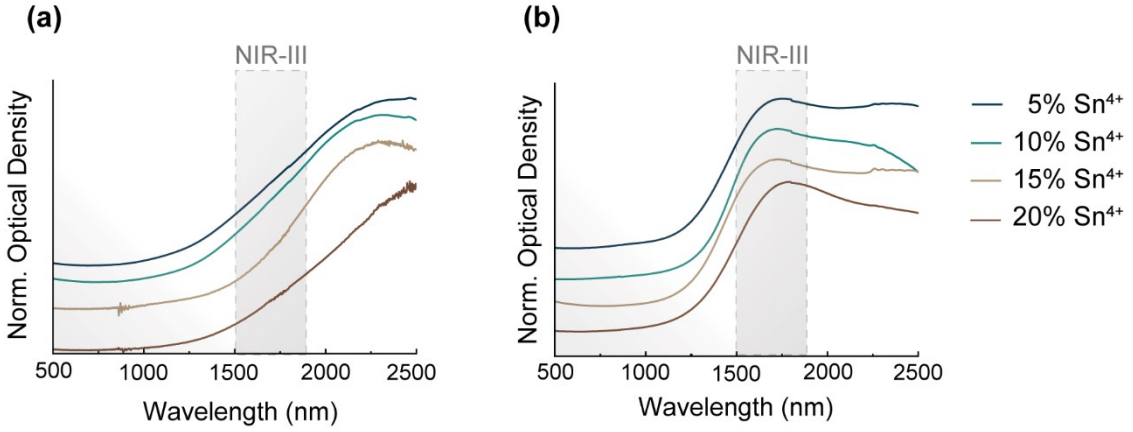

Figure S6. Normalized UV-VIS extinction spectra of ITO NPs using different Sn concentrations (5, 10, 15 and 20 %) and different organic acid ligands: (a) Octanoic acid and (b) benzoic acid. A vertical offset was

introduced to better distinguish the different spectral profiles. The grey rectangles in both spectra indicate the NIR-III biological window (1500-1850 m).

S6. TEM images of CuS nanoparticles

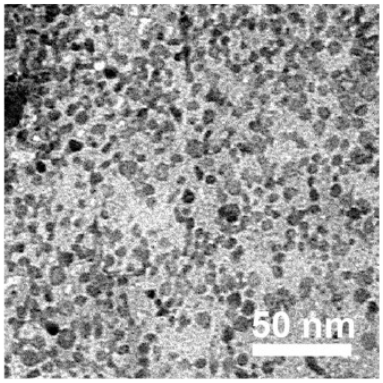

Figure S7. Representative TEM image of CuS NPs dispersed in water.

S7. TEM images of $NaGdF_4$: Nd^{3+} NPs (Nd-NPs)

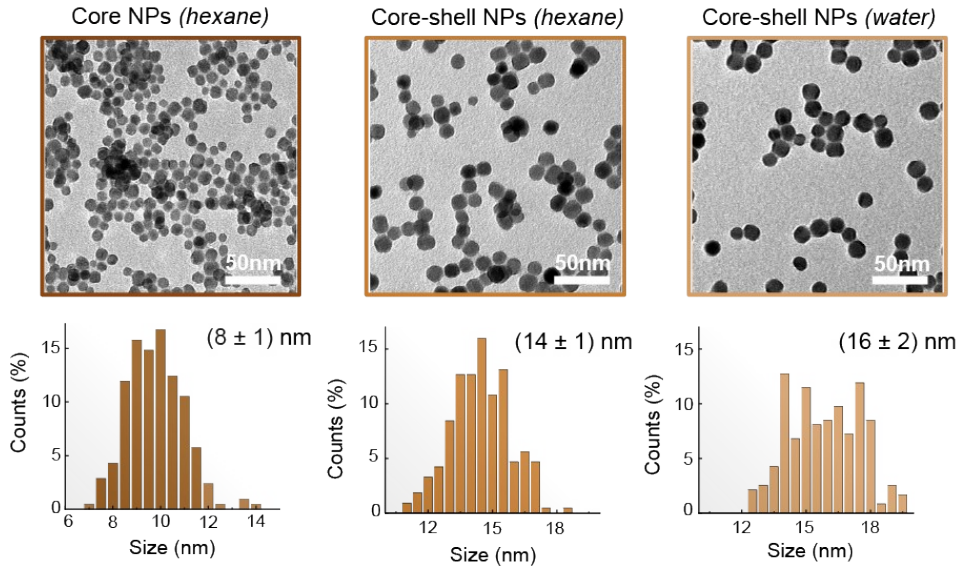

Figure S8. Representative TEM images with their respective size distribution of core $NaGdF_4$:Nd^{3+} NPs dispersed in hexane (left), core-shell $NaGdF_4$:Nd^{3+}@$NaGdF_4$ NPs dispersed in hexane (middle) and core-shell $NaGdF_4$:Nd^{3+}@$NaGdF_4$ NPs dispersed in water.

S8. Computational methodology and additional results

We computed the electromagnetic response of two types of ITO nanostructures using COMSOL Multiphysics, a commercial software package used to numerically solve differential equations using Finite Element Methods (FEM). The two geometries in **Figure S10** were illuminated by linearly polarized planewaves while immersed in a homogeneous dielectric medium with constant refractive index of $n = 1.33$, i.e. water. For materials well described by the Drude model of ballistic conduction, as it is the case of ITO, we can compute their permittivity through the expression

$$\varepsilon(\omega) = \varepsilon_\infty - \frac{\omega_p^2}{\omega(\omega + i\gamma)}$$

with ω_p being the plasma frequency of the conductor, and γ its damping rate. In our nanoparticle simulations, we have used experimentally available ITO permittivity, [4]and extrapolated these values to longer wavelengths after fitting the experimental data to the Drude model's expression above. Our fitting parameters were $\varepsilon_\infty = 3.89$, $\omega_p = 1.95\ eV$, and $\gamma = 0.853\ eV$. The resulting dataset is shown in **Figure S9.**

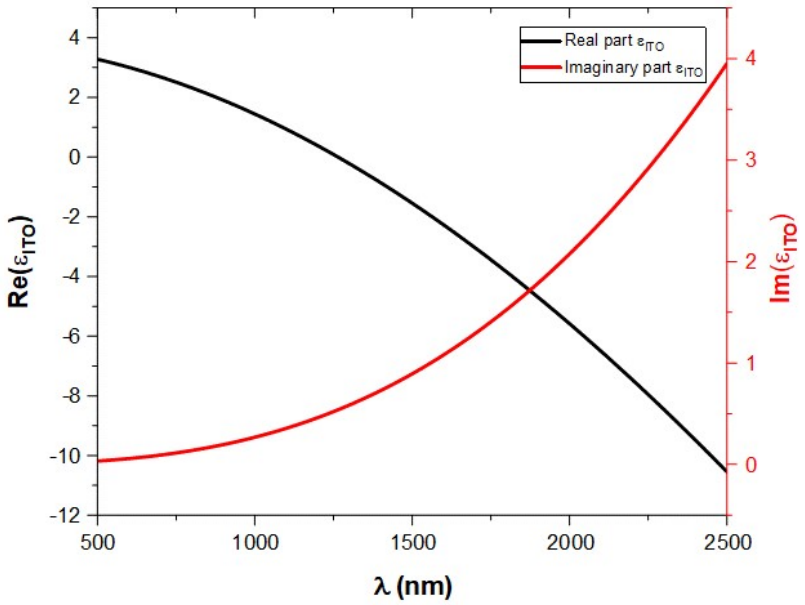

Figure S9. Real and imaginary part of the permittivity of ITO, as obtained from the Drude model with parameter obtained from fitting experimental data.

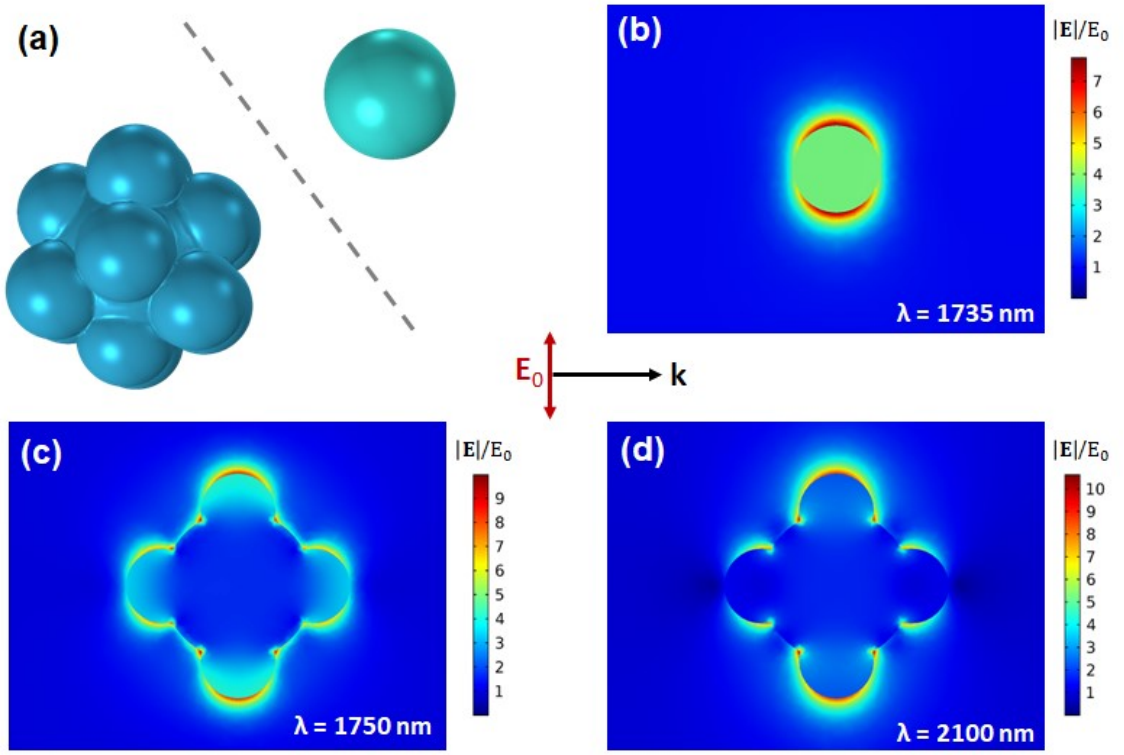

Figure S10. (a) Renders of the models used for the simulation of individual and aggregated nanostructures. (b-d) Cross sectional maps of the enhanced field created by the ITO systems, for the main plasmonic mode of the individual NP and the two main modes of the aggregated structure.

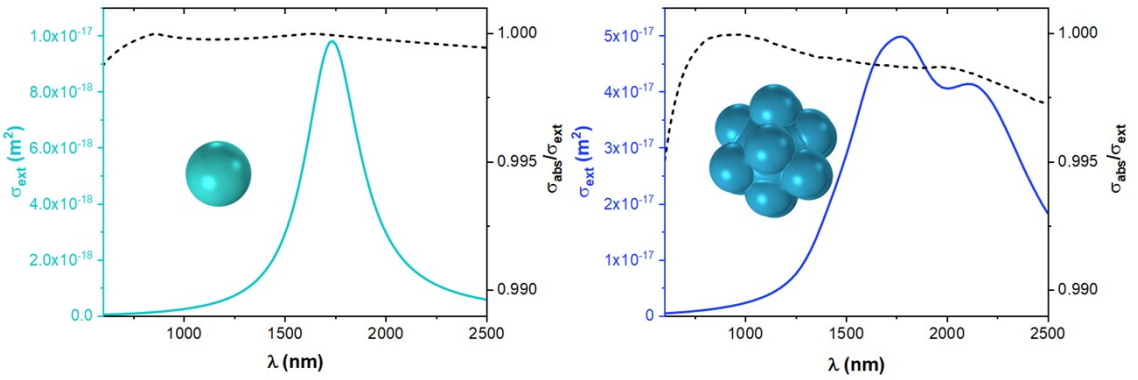

Figure S11. Computational results for the optical interaction cross sections of both individual (left) and aggregated (right) structures. Each panel shows extinction cross section spectrum (left axes) and the ratio of absorption to scattering cross sections (right axes). The values of 0.999 close to unity indicate that the practical totality of the energy of the plasmon is dissipated locally.

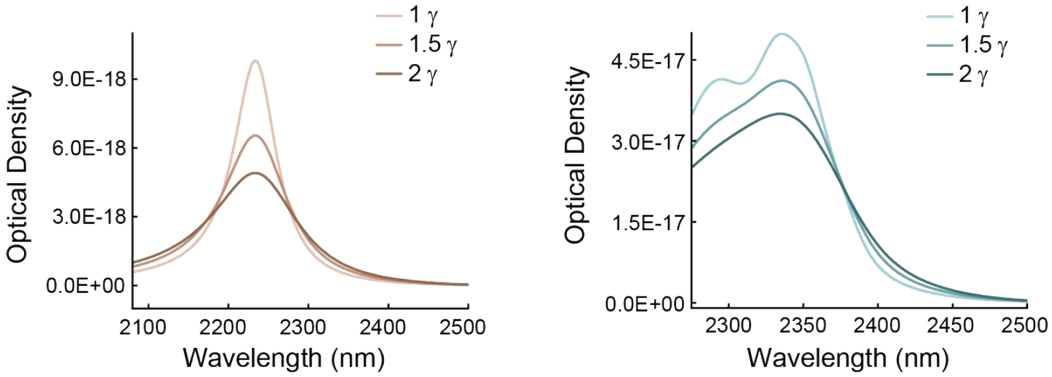

Figure S12. Calculated extinction spectra of a 7 nm ITO nanosphere (left) and an 18 nm agglomeration (right) of spherical ITO nanoparticles using three different effective scattering constants in the Drude model: the one obtained from the fitting of the experimental permittivity (1γ), and two that are multiples of γ (1.5γ, 2.0γ).

S9. Experimental heating efficiency

HCE droplet setup

Our system is composed of a 1718-nm laser used to irradiate the droplet, which in turn is hanging from a syringe needle. The beam size is adjusted with an iris diaphragm, so all the beam passes through the droplet. On the right-hand side is the power meter, which has been used to detect the power of the laser with and without hanging droplet. In addition, we have placed a germanium lens in front of the thermal camera to magnify the size of the droplet displayed in the camera.

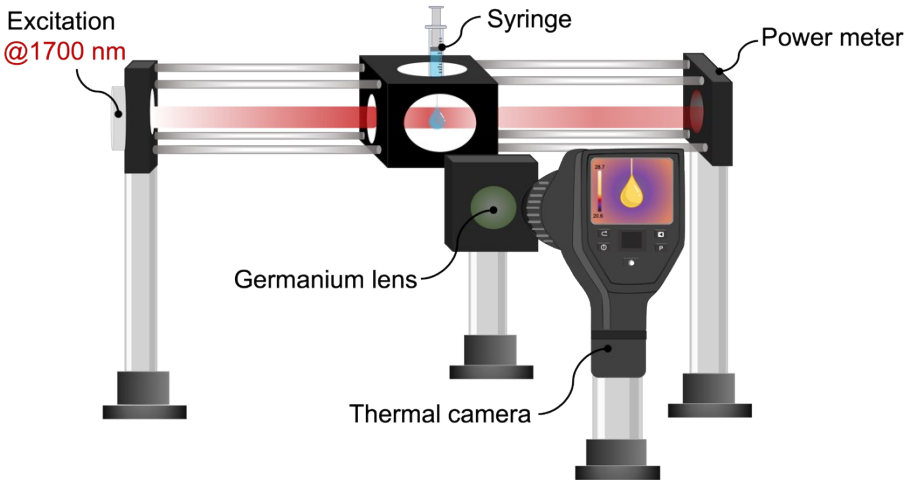

Figure S13. Droplet setup adapted from the work of Bednarkiewicz et al. [5]for the HCE measurements.

HCE data collection

To perform the experiment, temperature was recorded for at least 30 seconds before the 1718 nm laser was turned on, to have a starting baseline. Then, once the laser is illuminating the droplet, the temperature rises for a few seconds before stabilizing after approximately 2 minutes. Then, the laser was switched off, thus recording the cooling curve until the droplet returned to the initial temperature.

HCE calculations

For the determination of the heat conversion efficiency (HCE) value, we follow a macroscopic model described in a previously reported work. [5]The commonly used HCE equation is described as follows:

$$\eta = \frac{Q_{ext} - Q_0}{P_{H_2O}(1 - 10^{-O.D})}$$

η is the photothermal conversion efficiency, Q_0 is heat dissipated by the solvent alone, Q_{ext} is the external heat dissipated coming from absorption of the colloidal dispersion, P_{H_2O} is the incident infrared laser power and $O.D$ is the optical density of the NPs at the

wavelength selected for the irradiation of the sample. In this work, the absorbed infrared laser power (P) is evaluated from the difference between the outgoing infrared laser power on a drop of water P_{H_2O} and the outgoing infrared laser power on a drop of the sample P_{H_2O+ITO}, which were both detected with a power meter.

$$P = P_{H_2O}(1 - 10^{-O.D}) = P_{H_2O} - P_{H_2O+ITO}$$

The heat flux in the system follows the expression:

$$Q = hA(\Delta T)$$

where ΔT is the temperature increment (subtracting from the maximum temperature the room temperature of the droplet), h is the heat transfer coefficient and A is the area of the sample in contact with the surroundings. The product of hA is calculated as:

$$hA = \frac{\sum_i m_i C_{p,i}}{\tau}$$

where the m_i and $C_{p,i}$ are the mass and heat capacity of the material that compose the sample, τ is the sample time constant obtained by fitting the cooling part (to avoid the effects of thermal gradients during heating) of the heating-cooling curves.

Data from the thermal camera was recorded using FLIR E54 24º Tools software. Following the previous equations, we can calculate the heating efficiency. We averaged the results of three heating curves, both for the solvent and the ITO sample. For each calculation, we determined the mass of the droplet as the product of the water density (1 $g \cdot cm^{-3}$) and the volume of the droplet. The volume was calculated assuming a perfectly spherical droplet. The diameter of each droplet was determined from the thermal images, adequately calibrated in terms of size. A probe calibration sample was used to determine the size of the droplet (**Figure S14**). The τ is obtained by fitting an exponential decay function to the cooling part. The required parameters for HCE calculations are included in **table S15.**

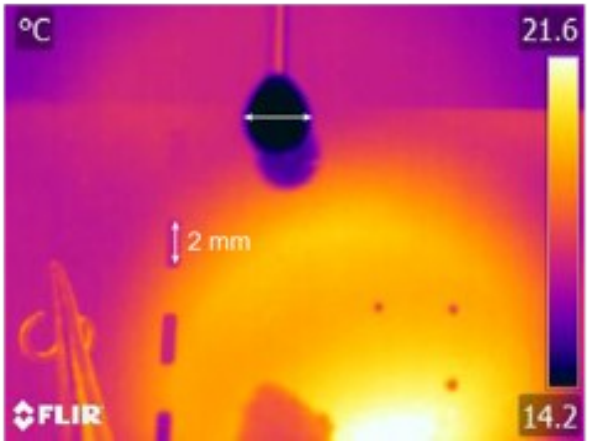

Figure S14. Image of a probe calibration sample for a droplet size calibration

Table S2. Detailed data of HCE experimental results.

Sample	***Mass, g***	***ΔT, ºC***	$\tau_{cooling}$***, s***	***Q, J·s⁻¹***
H_2O 1	0.0050	4.48	20.93	0.0041
H_2O 2	0.0040	4.43	17.87	0.0042
H_2O 3	0.0040	4.60	18.20	0.0041
ITO 1	0.0050	6.12	24.57	0.0050
ITO 2	0.0040	6.59	22.54	0.0052
ITO 3	0.0040	6.10	20.68	0.0046

Table S3. Detailed data of power density experimental results.

P_{H_2O}, W	P_{H_2O+ITO}, W
0.0064	0.0052
0.0068	0.0058
0.0072	0.0065

Table S4. Comparison of some HCE values for nanomaterials within the NIR-II and NIR-III.

Sample	**Wavelength (nm)**	**η, %**	**Reference**
ITO	1718	84	This work
CuO/Cu_2O NTCs	1550	78	[6]
BF_2 complex	1064	80	[7]
Gold nanodumbbells (AuNDs)	1064	84.9	[8]
CuS nanostructures	1064	≥ 72	[9]
AuDAg$_2$S nanoprobes	1064	67.1	[10]
H_2O_2-activated AuNCs@SiO_2	1064	82.2	[11]

R-Au/Pt-CdS	1064	38.9	[12]

S10. Penetration depth of the two different nanofluids:

The penetration depth of light is defined as the depth at which the radiation intensity inside the material decays by 1/e of its initial value. In this work, the penetration depth for each one of the two nanofluids studied is calculated following the Lambert-Beer equation:

$$\frac{I}{I_0} = e^{-l\alpha}$$

Where I is the transmitted intensity, I_0 is the incident intensity, α is the extinction coefficient, and l is the optical path.

That equation was applied as described below to elucidate the different extinction values represented for each plasmonic NPs - ITO or CuS ones - accompanying the Nd-NPs to form each nanofluid. Specifically, I_0 is the recorded luminescence intensity (around 1060 nm) from a colloidal dispersion of just Nd-NPs inside the microchannel under 800 nm laser excitation. In the other hand, I is the luminescence value recorded from each of the two nanofluids (Nd-NPs + CuS and Nd-NPs + ITO NPs) put alternatively inside the microchannel under 800 nm laser excitation.

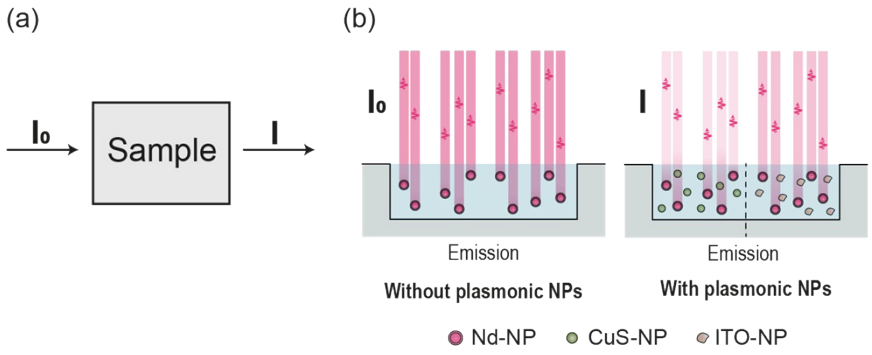

Figure S15. (a) General scheme of Lambert-Beer's law as usually explained on textbooks (b) Scheme portraying how I_0 and I (Nd-NPs luminescence signal intensities) have been sequentially recorded; for the latter, -at the right side- the dashed line represents the fact that two different measurements have been performed, one for each distinct nanofluid (Nd-NPs + CuS and Nd-NPs + ITO NPs, respectively).

The specific details of how the calculations were ran are the following: since the particles are emitting from different positions within the microchannel (total depth of 0.4 mm), we select as the average optical path the distance from the surface to the center of the microchannel (0.2 mm). In this way, the l is an estimated average length. Since the experimental geometry is the same for both samples, the penetration depth obtained in both cases can be compared fairly.

To estimate the penetration depth from each of the two nanofluids studied, α was first calculated. Following the previous equation, for our case this variable can be defined as

$$\alpha = \frac{-\ln(I)}{0.2\ mm}$$

Once the α value is determined (in units of mm^{-1}) for each one of the two nanofluids under study, the *penetration depth* of Nd^{3+} signal emission (d) is calculated as the inverse of the respective extinction coefficient in units of mm (in this work, it is purely absorption, as we consider the scattering caused by tiny NPs as negligible). Hence,

$$d = \frac{1}{\alpha}$$

The results obtained are included in the following table, directly writing down the $\frac{I}{I_0}$ value:

Table S5. Detailed data of parameters for the calculation of penetration depth

Nanofluid	I / I_0	α **, mm^{-1}**	***d, mm***
Nd^{3+}+ CuS	0.81	1.05	1.0
Nd^{3+}+ ITO	0.94	0.31	3.2

S11. Stability over time of ITO NPs dispersed in a complex medium of biological relevance

The stability over time of ITO NPs dispersed in a complex medium of biological relevance has been investigated: *Fetal Bovine Serum* (FBS). This is a widely used biological medium for *in vitro* studies that also contains families of organic and inorganic species that are generally found in biological environments:

a. Proteins, like albumin, responsible for NP opsonization
b. Salts shown to be responsible for colloidal destabilization (e.g., NaCl) and/or particle degradation (e.g., phosphates)
c. Other molecules like glucose, hormones, and vitamins.

In order to carry out the stability test, we prepared two different samples. The first sample contains a dispersion of ITO NPs [0.45 mg/mL] and FBS (10:90 volume proportion) and the second one, contains a solution of H_2O and FBS with the same volume proportion. Subsequently, we performed dynamic light scattering (DLS) measurements on the dispersion of ITO NPs in FBS. In **Figure S16a**, we can observe that the higher hydrodynamic size of the solution prepared with ITO NPs and FBS is due to the hydrodynamic size provided by the FBS itself. After this, we measured the hydrodynamic size over 8 days as shown in **Figure S16b**. While the hydrodynamic size changes when the particles are transferred from water to FBS, as expected due to the different electrostatic environment, no significant changes in the intensity-averaged hydrodynamic size are observed over time. This means that the ITO NPs are not only stable in water but also in a complex medium of biological relevance such as FBS.

Finally, to evaluate the extent of the potential change on the optical properties of ITO NPs induced by being dispersed in FBS, i.e. prolonged interaction between ITO NPs and such medium, we measured the optical extinction of these NPs. As shown in the extinction

spectra (**Figure S16c**), there is no peak shift of the ITO NPs when comparing the outcome from both distinct dispersions (upon 8 days of exposition of the ITO NPs to FBS, and in H_2O), thus supporting the fact of the stability from the optical standpoint of ITO NPs under dispersion in such biological medium.

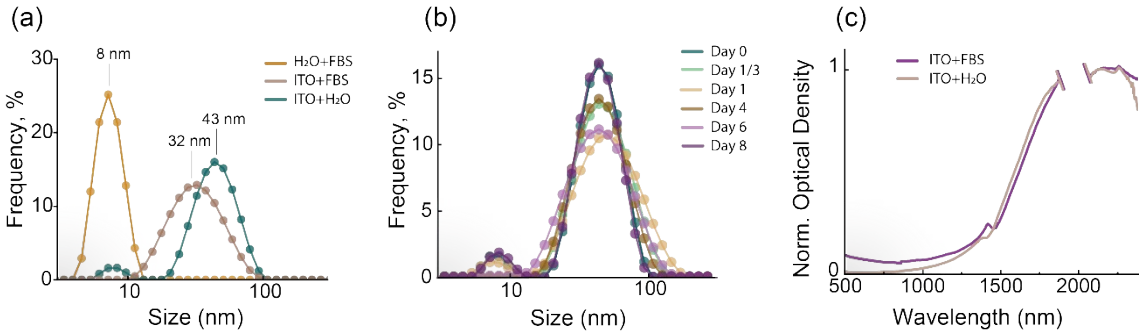

Figure S16. (a) Hydrodynamic size of FBS in water (yellow line), ITO NPs dispersed in FBS (brown line) and ITO NPs in water (green line), (b) hydrodynamic size of ITO NPs in FBS over approximately1 week, (c) Normalized UV-VIS extinction spectra of ITO NPs upon 8 days dispersed in FBS (purple line) and in water (brown line).

S12. Cell viability study

U87 MG cell line (glioblastoma, epithelial) was selected as representative cancer model to assess the toxicity of the obtained ITO nanoparticles functionalized with citrate Cells were incubated for 24h with different NP concentrations ranging from 20 to 200 ug/mL. The obtained results, following an MTT viability assay, are plotted in Figure S11. They show that upon increasing the NP concentration, the viability remained well above 70%, which is regarded as the limit below which a material at a specific concentration is considered cytotoxic (ISO-10993-5-2009). Indeed, a one-way ANOVA test performed on the data shows that differences are not statistically significant considering $p<0.05$.
As ITO nanoparticles are colloidally stable during the incubation period, it may be the case that they are not interacting with the cells. To check this point, ICP-MS measurements on the cells incubated with the NPs (after washing with PBS) were performed, indicating an internalization by the cells between 0.1 to 2.0% (0.8% on average), which guarantees their interaction.

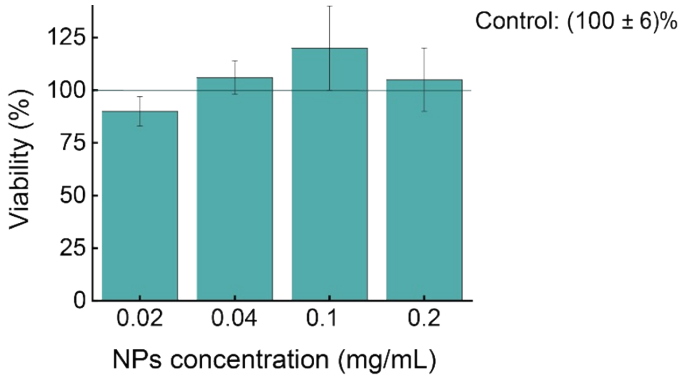

Figure S17. Viability results obtained in U87 MG cell line after 24 h treatment with different concentrations of ITO nanoparticles (n=4)

S13. References

1 F. Chen, H. Hong, S. Goel, S. A. Graves, H. Orbay, E. B. Ehlerding, S. Shi, C. P. Theuer, R. J. Nickles and W. Cai, *ACS Nano*, 2015, **9**, 3926–3934.
2 F. Wang, R. Deng and X. Liu, *Nat Protoc*, 2014, **9**, 1634–1644.
3 M. Kanehara, H. Koike, T. Yoshinaga and T. Teranishi, *J. Am. Chem. Soc.*, 2009, **131**, 17736–17737.
4 Y. Wang, A. Capretti and L. Dal Negro, *Opt. Mater. Express*, 2015, **5**, 2415.
5 A. Paściak, A. Pilch-Wróbel, Ł. Marciniak, P. J. Schuck and A. Bednarkiewicz, *ACS Appl. Mater. Interfaces*, 2021, **13**, 44556–44567.
6 M. Shanmugam, N. Kuthala, R. Vankayala, C.-S. Chiang, X. Kong and K. C. Hwang, *ACS Nano*, 2021, **15**, 14404–14418.
7 Z. Jiang, C. Zhang, X. Wang, M. Yan, Z. Ling, Y. Chen and Z. Liu, *Angew Chem Int Ed*, 2021, **60**, 22376–22384.
8 Y. Zhang, T. Song, T. Feng, Y. Wan, N. T. Blum, C. Liu, C. Zheng, Z. Zhao, T. Jiang, J. Wang, Q. Li, J. Lin, L. Tang and P. Huang, *Nano Today*, 2020, **35**, 100987.
9 G. Morgese, P. Dolcet, A. Feis, C. Gellini, S. Gialanella, A. Speghini, D. Badocco, P. Pastore, M. Casarin and S. Gross, *Eur J Inorg Chem*, 2017, **2017**, 2745–2754.
10 J. He, S. Hua, D. Zhang, K. Wang, X. Chen and M. Zhou, *Adv Funct Materials*, 2022, **32**, 2208028.
11 Y. Lu and M. Li, *Adv Funct Materials*, 2024, **34**, 2312753.
12 H. Yan, G. Li, F. Zhang, J. Liu and M. Luoshan, *Nanomaterials*, 2024, **14**, 838.